

CHANDRA SURVEY OF NEARBY GALAXIES: THE CATALOG

RUI SHE¹, LUIS C. HO^{2,3}, AND HUA FENG¹
Draft version December 28, 2016

ABSTRACT

We searched in the public archive of the *Chandra* X-ray Observatory as of March 2016 and assembled a sample of 719 galaxies within 50 Mpc with ACIS observations available. By cross-correlation with the optical or near-infrared nuclei of these galaxies, 314 of them are identified to have an X-ray active galactic nucleus (AGN). The majority of them are low-luminosity AGNs and are unlikely X-ray binaries based upon their spatial distribution and luminosity functions. The AGN fraction is around 60% for elliptical galaxies and early-type spirals, but drops to roughly 20% for Sc and later types, consistent with previous findings in the optical. However, the X-ray survey is more powerful in finding weak AGNs, especially from regions with active star formation that may mask the optical AGN signature. For example, 31% of the H II nuclei are found to harbor an X-ray AGN. For most objects, a single power-law model subject to interstellar absorption is adequate to fit the spectrum, and the typical photon index is found to be around 1.8. For galaxies with a non-detection, their stacked *Chandra* image shows an X-ray excess with a luminosity of a few times 10^{37} erg s⁻¹ on average around the nuclear region, possibly composed of faint X-ray binaries. This paper reports on the technique and results of the survey; in-depth analysis and discussion of the results will be reported in forthcoming papers.

Subject headings: galaxies: active – galaxies: nuclei – X-rays: galaxies

1. INTRODUCTION

It is widely accepted that every galaxy with a bulge harbors a central supermassive black hole (for a review see Kormendy & Ho 2013). Correlations between the mass of the central black hole (M_{BH}) and the properties of the bulge have been identified. For example, M_{BH} scales with the stellar mass or luminosity of the bulge (Kormendy & Richstone 1995; Magorrian et al. 1998), and with its stellar velocity dispersion (σ ; Gebhardt et al. 2000; Ferrarese & Merritt 2000). Among elliptical galaxies and classical bulges, both correlations are equally tight (Kormendy & Ho 2013). These correlations lead to the hypothesis that massive galaxies may have evolved along with their central black holes, perhaps linked by feedback from active galactic nuclei (AGNs; for reviews, see Alexander & Hickox 2012; Kormendy & Ho 2013; Heckman & Best 2014). However, whether the $M_{\text{BH}} - \sigma$ relation extends to lower mass black holes and galaxies is unclear. Compared with ellipticals and classical bulges, pseudobulges exhibit a significantly different $M_{\text{BH}} - \sigma$ relation, with larger scatter and lower normalization (Kormendy & Ho 2013; Greene et al. 2016). The situation for bulgeless galaxies is even more uncertain because the fraction of them that contains a central black hole is still undetermined. The bulgeless, late-type spiral NGC 4395 hosts a black hole with $M_{\text{BH}} \approx 10^5 M_{\odot}$ (Filippenko & Ho 2003; Peterson et al. 2005; den Brok et al. 2015), as does the dwarf spheroidal galaxy POX 52 (Barth et al. 2004). A systematic search of the Sloan Digital Sky Survey uncovered 200–300 new cases of low-

mass ($M_{\text{BH}} < 10^6 M_{\odot}$) black holes residing in low-mass galaxies (Greene & Ho 2004, 2007; Dong et al. 2012), but the statistical completeness of these optical searches are difficult to quantify (Greene & Ho 2009). As the case of M 33 illustrates (Gebhardt et al. 2001; Merritt et al. 2001), clearly not every late-type galaxy contains a central black hole.

The fraction of black holes in low-mass galaxies in the local universe can constrain the mechanism for the formation of the supermassive black holes in the early universe (Volonteri et al. 2008). Specifically, a higher black hole occupation fraction in low-mass ($M_{*} < 10^{10} M_{\odot}$) galaxies is expected if seed black holes were created through the collapse of Population III stars (Heger et al. 2003) instead of direct collapse of gas clouds (Haehnelt & Rees 1993). Based on a spectroscopic survey of a complete sample of nearby galaxies in the northern hemisphere, Ho et al. (1997a,b) report that the fraction of optical AGNs is as high as 60% for galaxies with a bulge component (Hubble types earlier than Sc), but drops to less than 20% for late-type (Sc or later) galaxies. AGN identification in the optical band may suffer from contamination by star formation, dust obscuration, and general dilution by host galaxy starlight. The problem is especially severe for galaxies with low-luminosity AGNs (LLAGNs).

The shortcomings of optical AGN searches can be alleviated, at least in part, by observations at other wavelengths. High-ionization lines (e.g., [Ne V] $\lambda 14.3 \mu\text{m}$) revealed through mid-infrared spectroscopy have successfully uncovered some weak AGNs in late-type galaxies previously missed in the optical (Satyapal et al. 2008; Dudik et al. 2009; Goulding & Alexander 2009). The sample sizes are, however, quite limited; moreover, the reliance on the detection of high-ionization lines automatically precludes the possibility of identifying low-ionization sources associated with low accretion rates (Ho

¹ Department of Engineering Physics and Center for Astrophysics, Tsinghua University, Beijing 100084, China

² Kavli Institute for Astronomy and Astrophysics, Peking University, Beijing 100087, China

³ Department of Astronomy, Peking University, Beijing 100087, China

2008, 2009). Radio cores can also effectively reveal weak nuclear activity, but the requisite observations at sub-mJy level sensitivity and sub-arcsecond resolution are not always available for large, homogeneous samples of galaxies (Filho et al. 2006).

X-ray observations, particularly at relatively hard energies (≥ 2 keV), provide an effective, robust means of identifying accretion-powered sources across a wide range of galaxy environments and level of nuclear activity. As stellar processes and hot gas also generate X-rays, even X-ray searches for AGNs are not immune from contamination by host galaxy emission. LLAGNs pose the greatest challenge. At sufficiently low accretion rates, even individual X-ray binaries can rival the signal from the weakest LLAGNs. However, host galaxy contamination can be minimized by taking advantage of the low background noise and superior angular resolution of the Advanced CCD Imaging Spectrometer (ACIS) onboard *Chandra* (Weisskopf et al. 2002), which has a point-spread function (PSF) with FWHM $\approx 0''.5$. ACIS is extraordinarily sensitive to point sources, even with relatively short exposures (few ks), and its sharp PSF enables us to pinpoint their possible association with nuclear activity in nearby galaxies if the absolute astrometry of the nucleus of the galaxy is well constrained. This strategy was successfully implemented by Ho et al. (2001), who conducted a snapshot survey of 24 nearby galaxies using *Chandra*/ACIS, and it has since been adopted in other studies aimed at obtaining a census of weak AGNs (e.g., Terashima & Wilson 2003; Dudik et al. 2005; Gallo et al. 2008; Miller et al. 2012).

The X-ray search technique has been particularly effective in identifying candidate LLAGNs, presumably low-mass black holes, in very late-type, low-mass galaxies. In a *Chandra* archival study of 64 nearby galaxies, Desroches & Ho (2009) found that 20%–25% of late-type spiral galaxies contain an X-ray core plausibly due to nonstellar activity. Zhang et al. (2009) assembled a larger sample consisting of 187 nearby galaxies observed with *Chandra* and detected 86 X-ray AGNs, giving a fraction of $\sim 46\%$. They also found a dramatic drop of the AGN fraction, from $\sim 60\%$ in early-type galaxies to $\sim 30\%$ in late-type galaxies, but they did not address the association of AGNs with bulgeless galaxies. Greene (2012) presented preliminary results on the black hole occupation rate in low-mass galaxies using X-ray AGNs in nearby galaxies identified by Desroches & Ho (2009) and Gallo et al. (2010). Miller et al. (2015), based on X-ray observations of ~ 200 optically selected early-type galaxies, obtained a lower limit of 20% for the occupation fraction for early-type galaxies ($< 10^{10} M_{\odot}$).

This work conducts the largest, most comprehensive X-ray survey to date of nuclear black holes in a sample of 719 galaxies within 50 Mpc, using data from the *Chandra* archive. Our primary goal is to quantify the incidence of AGN activity as a function of Hubble type, with special emphasis on low-mass, late-type galaxies. Our sample is ~ 3 times larger than the largest previous one of its kind. In addition to searching for low-mass black holes in late-type galaxies, this survey will yield fruitful scientific results in many other aspects. For example, the study can help constrain the accretion models of LLAGNs (for a review see Yuan & Narayan 2014) and test whether the presence of a bar is essential for trig-

gering AGN activity (Kormendy & Kennicutt 2004). We will also investigate non-nuclear X-ray sources, in particular ultraluminous X-ray sources (Feng & Soria 2011). Our study will appear as a series of several papers, each focusing on a specific topic. This paper will discuss the sample construction and spectral classification (§ 2), X-ray data reduction (§ 3), statistical properties (§ 4), spectral properties (§ 5), and contamination by X-ray binaries (§ 6).

2. SAMPLE ASSEMBLY

The sample was assembled based on *Chandra*/ACIS observations that were publicly available as of March 2016. We first generated a full list of ACIS observations, and then searched in the NASA/IPAC Extragalactic Database⁴ (NED) for galaxies within 50 Mpc whose nuclear positions were less than $8'$ from the aim point of any *Chandra* observation. The adopted distances were taken from NED, in the following order of priority: surface brightness fluctuations, Cepheids variables, tip of the red giant branch, Type Ia supernovae, the fundamental plane, Faber-Jackson relation, Tully-Fisher relation, Tully estimate, and D-Sigma relation (for a review see Jacoby et al. 1992). If more than one reference is available for the distance by the same means, the latest one is selected, unless otherwise specified.

Whenever possible, we obtain positions of the galaxy nuclei based on measurements from near-infrared images, which suffer from less obscuration by dust or confusion from young star-forming regions. Most of the data come from the Two-Micron All Sky Survey (2MASS) extended source catalog (Skrutskie et al. 2006), or NED otherwise. In a few cases, the NED positions come from radio observations⁵. We discarded galaxies whose nuclear positions in NED were obtained from X-ray observations. The task *dmcoords* in CIAO was used to check whether every galaxy was in the *Chandra* field of view, followed by visual confirmation.

This results in a sample of 719 galaxies with 1559 ACIS observations, including 196 objects having multiple observations. The longest exposure was selected for galaxies with multiple observations.⁶ We checked for the CCD pileup effect following the *Chandra* ABC Guide to Pileup⁷. For M 58, M 87, and M 106, we chose observations (ObsID 406, 1808, and 2340, respectively) with a shorter frame time (0.4 s), in which the pileup effect was reduced to a negligible level. For many others⁸, the pileup effect is significant even if observations with a shorter frame time or a larger off-axis angle are available. We ran ray-tracing simulations for *Chandra* using MARX (Davis et al. 2012) and found that the pileup at the observed level did not lead to a bias in the source positioning. Thus, for these objects we used the ACIS

⁴ <http://ned.ipac.caltech.edu>

⁵ Circinus, M 51a, M 58, NGC 1156, NGC 3079, NGC 5128, NGC 5353

⁶ By coadding all available observations for each galaxy, we find that, for 90% of the galaxies without an AGN detection, the improvement in sensitivity is less than a factor of 3 compared to the longest exposure. Thus, coadding exposures will not improve the detection rate significantly and is not adopted for simplicity.

⁷ http://cxc.harvard.edu/ciao/download/doc/pileup_abc.pdf

⁸ Circinus, M 77, M 81, NGC 1052, 2992, 3998, 4051, 4151, 4203, 5128, 5506, 6300, 7172, and NGC 7314.

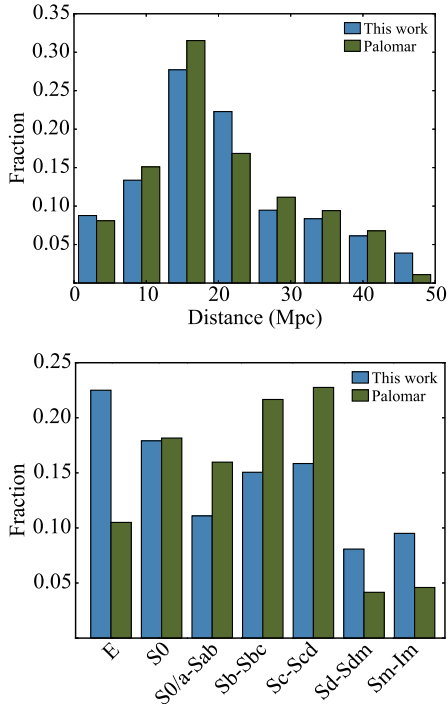


Figure 1. Distribution of the distances (top) and Hubble types (bottom) for objects in our sample (blue) and the Palomar survey (green).

image only for astrometric measurements; but the X-ray spectral properties of these sources were derived from published *XMM-Newton* or *ASCA* data. All of these targets are bright and well-studied AGNs and do not affect the main result of this study, which focuses on weak or previously unknown AGNs.

The general properties of the galaxies in our sample are listed in Table 1. The Hubble types were adopted from NED, which, in turn, are largely taken from the Third Reference Catalogue of Bright Galaxies (RC3; de Vaucouleurs et al. 1991). The $H\alpha$ luminosities were recalculated using the $H\alpha$ fluxes from the Palomar spectroscopic survey of bright galaxies (Ho et al. 1997a, 2003) and the distances given in Table 1. There are 419 galaxies in our sample that have published central stellar velocity dispersions σ_* and their associated uncertainties: 249 objects from the Palomar survey (Ho et al. 2009), 163 objects from the HyperLeda database⁹, and 7 objects from Gu et al. (2006).

The distributions of the distances and Hubble types for objects in our sample are compared to those in the Palomar survey (Ho et al. 1997b) in Figure 1. The Palomar survey is a complete sample of galaxies in the northern hemisphere brighter than 12.5 mag in the B band. The distances for objects in our sample do not show an apparent deviation from those in the Palomar sample. Compared with the Palomar survey, our sample contains a higher fraction of ellipticals and irregular galaxies and has a slightly lower abundance of early-type spirals.

In our sample, 249 galaxies have nuclear optical spectral classifications available in the Palomar survey (Ho et al. 1997a). Nuclear spectral classifications for another

44 galaxies were found in the catalog of Véron-Cetty & Véron (2010). For galaxies whose spectral classifications are not included in these two catalogs, we adopted nuclear emission-line fluxes from Moustakas & Kennicutt (2006) for 22 objects. In addition, we collected relatively high-quality optical spectra for 103 objects from the literature (Kennicutt 1992; Falco et al. 1999; Colless et al. 2003; Jones et al. 2009; Rosales-Ortega et al. 2010; Driver et al. 2011) and performed spectral fitting to determine their spectral classification. The spectra were fitted using GANDALF¹⁰ with Gaussians for the emission lines and a continuum component composed of optimally combined stellar templates of various ages (Bruzual & Charlot 2003). The nuclear spectral classifications were then performed using the diagnostic diagrams defined in Ho et al. (1997a) based on emission-line intensity ratios ($[\text{O III}] \lambda 5007 / H\beta$ versus $[\text{N II}] \lambda 6583 / H\alpha$, $[\text{S II}] \lambda \lambda 6716, 6731 / H\alpha$, and $[\text{O I}] \lambda 6300 / H\alpha$)¹¹, shown in Figure 2. (We note that most of the newly analyzed optical spectra are not flux calibrated, so that absolute fluxes of the emission lines are not available.) To summarize: 418 out of 719 galaxies in our sample have a nuclear optical spectral classification (for a review see Ho 2008), including 59 Seyferts, 66 low-ionization nuclear emission-line regions (LINERs; Heckman 1980), 41 transition objects (emission-line nuclei with $[\text{O I}]$ strengths intermediate between those of $H\text{II}$ nuclei and LINERs; see Ho et al. 1993), 163 $H\text{II}$ nuclei, and 89 absorption-line nuclei (those without optical emission lines).

3. X-RAY DATA REDUCTION

The ACIS data were reduced using CIAO 4.5 with CALDB 4.5.7. New level 2 event files were generated using the task *chandra_repro*. Intervals with background flaring were excluded using the task *lc_clean*. For most observations, intervals with background fluxes 1.2 times above or below the mean flux were rejected, as recommended. For those with heavy flares, *lc_sigma_clip* was used instead, and intervals where the flux was over $\pm 3\sigma$ fluctuation of the mean were excluded. The task *fluximage* was used to extract exposure-corrected images and exposure maps over the energy range 0.3–8 keV from the cleaned event files. A power-law spectrum with a photon index $\Gamma = 1.7$, typical for AGNs in nearby galaxies (Ho 2008), subject to Galactic absorption along the line-of-sight (Kalberla et al. 2005) was used as a weight for the exposure map. The task *mkpsfmap* was used to create a map for the PSF sizes (radii enclosing 39.3% of the PSF power) at the average energy of the weighting spectrum for each observation. Source detection was performed with *wavdetect*, which generated source regions that enclose 98.9% (3σ) of the total counts for spectral extraction.

We consider a compact X-ray source to be a candidate AGN if its X-ray position is spatially coincident with the near-infrared/optical position of the stellar nucleus of the galaxy at 99% confidence level. The relative po-

¹⁰ GANDALF was developed by the SAURON team and is available from the SAURON website (www.strw.leidenuniv.nl/sauron); see Sarzi et al. (2006) for details.

¹¹ In cases when the three diagrams give inconsistent results, the same classification given by two of them was chosen; if none is the same or the other two give ambiguous results, the classification based on $[\text{O I}]$ was chosen.

⁹ <http://leda.univ-lyon1.fr>

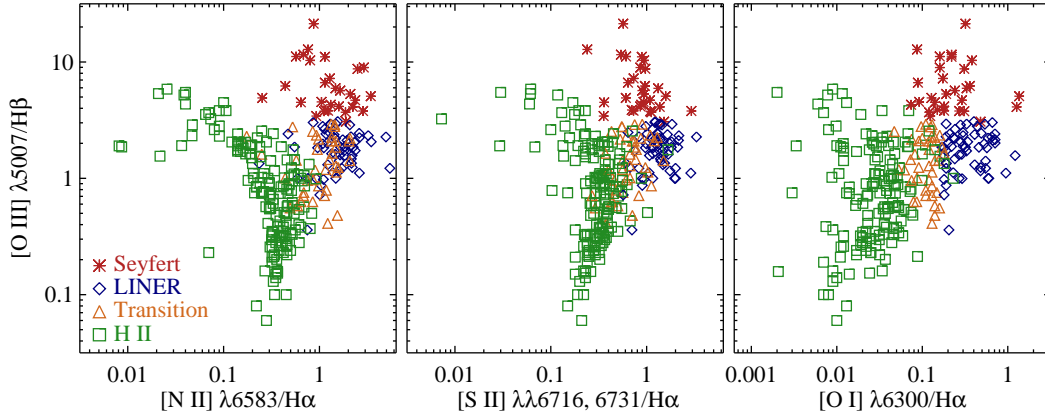


Figure 2. Emission-line diagnostic diagrams for nuclear optical spectral classifications for objects in our sample.

Table 1
general information for galaxies in our sample

ID	Name	Distance	R.A.	Dec.	Class	Hubble Type	σ_*	$\log L_{H\alpha}$	$\log M_{BH}$	$N_{H,0}$
(1)	(2)	(Mpc)	(J2000)	(J2000)	(6)	(7)	(km s^{-1})	(erg s^{-1})	(M_{\odot})	(10^{22} cm^{-2})
1	AM 0337-353	18.9	03:39:13.30	-35:22:17.2	...	dSAB0 ⁰ ?(s)	0.0158
2	AM 1247-410	36.6	12:50:07.74	-41:23:52.8	0.0848
3	AM 1318-444	3.96	13:21:47.40	-45:03:42.0	...	IBm	0.0705
4	ARK 65	10.8	01:56:12.01	+05:35:18.9	0.0435
5	ARP 244	21.5	12:01:53.17	-18:52:37.9	0.0315
6	ARP 261 NED01	28.8	14:49:30.58	-10:10:23.9	...	IB(s)m pec	0.0785
7	CCC 61	44.2	12:48:39.69	-41:16:05.6	0.0854
8	CCC 111	37.7	12:49:40.14	-41:21:58.3	0.0848
9	CCC 123	37.3	12:49:56.00	-41:24:04.4	0.0848
10	Circinus Galaxy	4.21	14:13:09.95	-65:20:21.2	...	SA(s)b?	0.5589
11	DDO 180	22.7	13:38:10.32	-09:48:06.6	...	SB(s)m	0.0319
12	Draco Dwarf	0.093	17:20:12.39	+57:54:55.3	...	E pec	0.0225
13	Dwingeloo 1	5.3	02:56:50.96	+58:54:38.8	0.7678
14	ESO 121- G 20	6.08	06:15:54.19	-57:43:31.6	...	dwarf	0.0378
15	ESO 137- G 6	41.6	16:15:03.86	-60:54:26.1	...	E1	355.5 ± 15.3	...	$9.61^{+0.10}_{-0.10}$	0.1747
16	ESO 138- G 10	14.7	16:59:02.95	-60:12:57.7	...	SA(s)dm	0.1444
17	ESO 233- G 35	47.1	20:09:25.61	-48:17:05.2	...	S0	0.0390
18	ESO 293-IG 034	20.9	00:06:19.91	-41:29:59.7	...	SB(s)cd pec	0.0132
19	ESO 322- G 93	47.7	12:49:04.15	-41:20:20.4	...	S?	0.0854
20	ESO 322- G 102	30.5	12:49:37.84	-41:23:17.6	...	SB0 ⁰ (s)?	104.6 ± 3.7	...	$6.85^{+0.08}_{-0.08}$	0.0848

Note. — Column 1: Source ID. Column 2: Galaxy names. Column 3: Distance from NED. Column 4: Right ascension of galaxies in J2000. Column 5: Declination of galaxies in J2000. Column 6: Spectral classification. “.” and “:” indicate a classification which is uncertain and highly uncertain, respectively, (Ho et al. (1997a)). Column 7: Hubble type from NED. Column 8: Velocity dispersion. Column 9: $H\alpha$ luminosity from the Palomar survey (Ho et al. 1997a, 2003). The typical uncertainties is 10-30%, and the letters “b”, “c”, “l” and “u” indicate an uncertainty of 30-50%, 100%, a 3σ lower limit, and a 3σ upper limit, respectively. Column 10: Black hole masses estimated using the $M_{BH} - \sigma$ relation. More details are in the text. Column 11: Galactic absorption column density. Table 1 is published in its entirety in the machine-readable format. A portion is shown here for guidance regarding its form and content.

sition uncertainty of an X-ray source with respect to its near-infrared/optical counterpart consists of three components: the near-infrared/optical position error, the absolute astrometry of *Chandra*, and the statistical error for the X-ray position. For most objects, the position of the galaxy center is adopted from the 2MASS catalog for extended sources. In 2MASS near-infrared images, the stellar nucleus often appears extended, and the 1σ position error on the peak is quoted as $0''.5$ (Jarrett et al. 2000). Assuming a Rayleigh distribution, this can be translated to a 99% position uncertainty $\Delta_{2MASS} = 3.05\sigma = 1''.525$ in radius. The absolute *Chandra* astrometry¹² for ACIS is $\Delta_{CXC} = 0''.8$ on-axis at a confidence level of 99%. For sources at an off-axis angle greater than $3'$, an additional position error due to PSF blurring and asymmetry is

introduced, roughly equal to 1/4 of the 50% encircled energy radius at the corresponding off-axis angle. The 99% statistical error radius from source detection given by *wavdetect* is denoted as Δ_{STA} , which is often much smaller than Δ_{CXC} and Δ_{2MASS} . Therefore, the total relative position uncertainty between the X-ray and near-infrared/optical positions at a 99% confidence level can be expressed as $\Delta_{99\%} = \sqrt{\Delta_{CXC}^2 + \Delta_{STA}^2 + \Delta_{2MASS}^2}$.

We also compared the NED positions with the 2MASS positions and found that 20 galaxies have a deviation larger than $2''$. Most of them are late-type galaxies with NED positions derived from optical images. As discussed above, we choose to trust the 2MASS positions in these cases, except for two objects discussed below. The nucleus of NGC 3621 looks like a point-like source on 2MASS images, and the position from the 2MASS

¹² <http://cxc.harvard.edu/cal/ASPECT/celmon/>

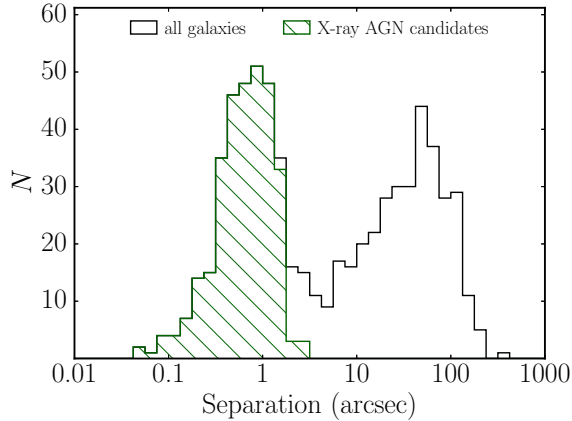


Figure 3. Distribution of the angular distance between the near-infrared or optical nucleus and the nearest point-like X-ray source on the sky plane. The open histogram is for all galaxies in our sample, while the hatched histogram is for AGN candidates, whose X-ray position is coincident with the near-infrared/optical nucleus at 99% confidence level.

extended source catalog may not be reliable. The nuclear position from NED is consistent with that in the 2MASS point source catalog, and coincident with an X-ray source. This object is then classified as an AGN candidate. NGC 891 is a nearly edge-on spiral, and the nucleus is masked by a dust lane, which is visible on 2MASS images even in the K_s ($2.16 \mu\text{m}$) band, challenging the validity of using its position. On *Spitzer* images at $3.6 \mu\text{m}$, the dust lane is gone, and the centroid of the nucleus is found to be R.A. = $2^{\text{h}}22^{\text{m}}33^{\text{s}}.03$, Dec. = $+42^{\circ}20'53''.2$ (J2000.0), which is $0''.76$ away from the 2MASS position for extended sources. We therefore quote this as the center for NGC 891. An X-ray counterpart is found around it and is still classified as an AGN candidate.

The distribution of the angular separation between the near-infrared or optical nucleus and the nearest point-like X-ray source is shown in Figure 3. The distribution is bimodal, with one peak centered near $0''.9$ and the other near $50''$. The distribution for X-ray AGN candidates, whose separation is less than $\Delta_{99\%}$, is also displayed (hatched histogram). The angular separations, less than $1''$ for most AGN candidates, are listed in Table 2.

3.1. Count Rates and Hardness Ratios

Source photons were extracted from the regions defined by *wavdetect*. The background was estimated from a concentric annulus surrounding the source ranging from $5''$ to $10''$ for most cases, or from another circular region if there is source confusion in the annulus. The net count rates and their associated errors were estimated assuming Poisson distributions for events in both the source and background regions. Given the counts, areas, and fractions of PSF powers in both the source and background apertures, the task *aprates* was used to calculate the net count rate and its 90% error bound with the Bayesian approach. In our cases, the PSF fraction is 0.989 in the source region and assumed to be 0 in the background region. For objects with no AGN identification, a circular source aperture with a radius that encloses 90% of the energy centered at the near-infrared/optical position of the nucleus was used to estimate the 90% upper limit of the source count rate using the task *aprates*.

We calculated the hardness ratios H_0 , H_1 and H_2 , defined as $H_0 \equiv (C_H - C_M - C_S)/C_T$, $H_1 \equiv (C_M - C_S)/C_T$, and $H_2 \equiv (C_H - C_M)/C_T$, where C_S , C_M , C_H , and C_T are counts in the soft band (0.3–1 keV), medium band (1–2 keV), hard band (2–8 keV), and full band (0.3–8 keV), respectively. The hardness ratio H_0 was used to infer the intrinsic hydrogen absorption column density $N_{\text{H,HR}}$ assuming a fixed photon index of $\Gamma = 1.8$, a typical value measured in this work (see § 5.2). We estimate the uncertainty of $N_{\text{H,HR}}$ by varying Γ between 1.3 and 2.3, which encompasses most of the values observed in this work.

3.2. X-ray Spectra

X-ray spectra were extracted for AGN candidates that have at least 100 photons in the energy range 0.3–8 keV, from the source and background regions defined above. The task *spectextract* was employed to extract the energy spectra, which were grouped to have at least 15 counts in each spectral bin and fitted in XSPEC 12.8 (Arnaud 1996). We first tried a simple power-law model subject to interstellar absorption with one absorption component fixed at the Galactic value (Kalberla et al. 2005) and a second free component to account for extragalactic absorption. If the single power-law model was inadequate to fit the data, resulting in a null hypothesis probability less than 0.05, we tried to add a thermal plasma component (*mekal*) or a cool blackbody component (*bbbody*), or we replaced the simple absorption model with a partial absorption model, and then tested the significance of the additional component with the F-test (being significant if the chance probability is < 0.05). The two-component model was found to be able to fit most of the spectra adequately. The extragalactic component was removed if the column density for the extragalactic absorption component converged to 0.

3.3. Flux, Luminosity, and Eddington Ratio

For AGN candidates with sufficient photons for spectral fitting, the observed flux, intrinsic luminosity, and their associated errors in the 2–10 keV band were calculated using the *cflux* model in XSPEC. For those without enough photons for spectral fitting, the flux and luminosity were translated from their source count rate assuming an absorbed power-law model, in which the photon index is fixed at two extremes $\Gamma = 1.3 - 2.3$ (for interval estimate), the absorption is inferred from the observed hardness ratio H_0 ($N_{\text{H,HR}}$, see above) and fixed at it, and the local detector response adopted is with the corresponding Γ . For non-detections in the nuclear region, the 90% upper limit on the source count rate was converted to an upper limit in flux and luminosity assuming an absorbed power-law spectrum with a photon index $\Gamma = 1.8$ and Galactic $N_{\text{H},0}$ based on the local detector responses.

The majority of the objects in our sample do not have a direct measurement of the black hole mass. We thus estimated the mass of black holes using the $M_{\text{BH}} - \sigma$ relation. As discussed by Kormendy & Ho (2013), the scaling relations between black hole mass and bulge properties are tight only for classical bulges and elliptical galaxies; pseudobulges show considerably more scatter and an apparently lower zero point. Kormendy & Ho (2013) provide

Table 2
X-ray properties for galaxies in our sample

ID	Name	Obsid	Inst	Exposure (ks)	Offset (")	AGN	H_0	H_1	H_2	$N_{\text{H,HR}}$ (10^{22} cm^{-2})	F_X (10^{-14} cgs)	$\log L_X$ (erg s^{-1})	Note
(1)	(2)	(3)	(4)	(5)	(6)	(7)	(8)	(9)	(10)	(11)	(12)	(13)	(14)
1	AM 0337-353	624	ACIS-S	43.6	...	N	<0.75	<37.52	G1.8
2	AM 1247-410	8179	ACIS-S	29.8	...	N	<0.14	<36.49	G1.8
3	AM 1318-444	15200	ACIS-I	19.5	...	N	<0.41	<36.60	G1.8
4	ARK 65	2223	ACIS-S	30.4	...	N	<0.73	<37.65	G1.8
5	ARP 244	3041	ACIS-S	72.9	...	N	<0.04	<35.85	G1.8
6	ARP 261 NED01	5191	ACIS-S	55.0	...	N	<0.13	<37.28	G1.8
7	CCC 61	16223	ACIS-S	179.0	...	N	<0.12	<38.21	G1.8
8	CCC 111	8179	ACIS-S	29.8	...	N	<0.37	<38.52	G1.8
9	CCC 123	8179	ACIS-S	29.8	...	N	<0.12	<37.63	G1.8
10	Circinus Galaxy	12823	ACIS-S	152.4	0.35	Y	0.484 ± 0.005	0.203 ± 0.006	0.511 ± 0.005	$1.73^{+0.68}_{-0.64}$	1400.00	42.20	Ref.2
11	DDO 180	6323	ACIS-S	7.1	...	N	<0.51	<38.23	G1.8
12	Draco Dwarf	9568	ACIS-S	24.5	...	N	<0.20	<32.95	G1.8
13	Dwingeloo 1	7151	ACIS-I	25.3	...	N	<0.20	<36.53	G1.8
14	ESO 121- G 20	14351	ACIS-I	26.2	...	N	<0.62	<36.70	G1.8
15	ESO 137- G 6	8178	ACIS-S	57.4	0.29	Y	-0.856 ± 0.009	-0.008 ± 0.018	-0.388 ± 0.016	<0.01	$5.24^{+1.11}_{-0.81}$	$39.92^{+0.10}_{-0.13}$	Fit
16	ESO 138- G 10	14800	ACIS-S	9.8	...	N	<0.26	<37.52	G1.8
17	ESO 233- G 35	3191	ACIS-I	23.5	...	N	<2.17	<39.49	G1.8
18	ESO 293-IG 034	11236	ACIS-S	9.9	1.29	Y	0.130 ± 0.205	0.217 ± 0.202	0.217 ± 0.202	$1.11^{+1.17}_{-0.82}$	$1.91^{+1.10}_{-0.81}$	$39.45^{+0.45}_{-0.38}$	HR
19	ESO 322- G 93	16223	ACIS-S	179.0	0.25	Y	-0.300 ± 0.122	0.500 ± 0.111	-0.233 ± 0.125	<0.63	$0.08^{+0.07}_{-0.07}$	$38.46^{+0.32}_{-0.48}$	HR
20	ESO 322- G 102	8179	ACIS-S	29.8	...	N	<0.61	<38.62	G1.8

Note. — Column 1: Source ID. Column 2: Galaxy names. Column 3: Chandra observation ID. Column 4: Focal plane instrument. Column 5: Exposure time. Column 6: Offset from the nearest point-like x-ray source to the optical position of the galaxy nucleus. Column 7: The galaxy has an AGN or not. Columns 8-10: Hardness ratios, defined as $H_0 \equiv (C_H - C_M - C_S)/C_T$, $H_1 \equiv (C_M - C_S)/C_T$, and $H_2 \equiv (C_H - C_M)/C_T$, where C_S , C_M , C_H , and C_T are counts in the soft band (0.3–1 keV), medium band (1–2 keV), hard band (2–8 keV), and full band (0.3–8 keV), respectively. Column 11: Intrinsic absorption inferred from hardness ratio. Column 12: Observed flux or 90% upper limit in the energy band of 2–10 keV. Column 13: Log of 2–10 keV luminosity, or 90% upper limits. Column 14: Note for X-ray luminosity. “Fit”, “HR” and “G1.8” denote luminosity from spectral fitting, hardness ratio, and assumption of $\Gamma=1.8$ with Galactic $N_{\text{H},0}$, respectively. For sources suffering from pileup, the references are given: Ref.1: [Ebrero et al. \(2011\)](#), Ref.2: [De Rosa et al. \(2012\)](#), Ref.3: [Cappi et al. \(2006\)](#), Ref.4: [Shu et al. \(2010\)](#), Ref.5: [Iyomoto et al. \(1998\)](#), Ref.6: [Ptak et al. \(2004\)](#), Ref.7: [Weaver et al. \(1999\)](#), Ref.8: [Guainazzi et al. \(2010\)](#), Ref.9: [Evans et al. \(2004\)](#). Table 2 is published in its entirety in the machine-readable format. A portion is shown here for guidance regarding its form and content.

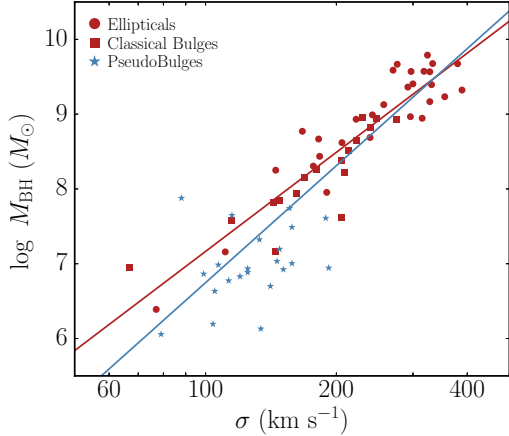


Figure 4. Black hole masses versus central stellar velocity dispersions (data adopted from Kormendy & Ho 2013). The blue line is the linear regression for all objects, while the red line is the fit for elliptical galaxies and classical bulges.

an updated $M_{\text{BH}} - \sigma$ relation only for classical bulges and ellipticals; they did not explicitly fit the pseudobulges, or their sample as a whole with all objects combined. We do not have bulge type classifications for the majority of our sample, but we can be certain that it contains both bulge types, as many of our objects have relatively late Hubble types, which preferentially host pseudobulges (e.g., Kormendy & Kennicutt 2004). In order to be able to estimate black hole masses from stellar velocity dispersions, we fit a single $M_{\text{BH}} - \sigma$ relation for all galaxies (independent of bulge type) deemed by Kormendy & Ho (2013) to have a reliable black hole mass measurement, using black hole masses and stellar velocity dispersions as tabulated by those authors. We performed the linear regression using the $(x|y)$ type bivariate correlated errors and intrinsic scatter (BCES) method (Akritas & Bershady 1996; Kelly 2007). Errors on both sides and an intrinsic scatter of the relation were taken into account. The regression results in the relation shown in Figure 4:

$$\log\left(\frac{M_{\text{BH}}}{M_{\odot}}\right) = - (0.68 \pm 0.05) + (5.20 \pm 0.37) \log\left(\frac{\sigma}{200 \text{ km s}^{-1}}\right) \quad (1)$$

with an intrinsic scatter of 0.44 dex. If we restrict the fit to just ellipticals and galaxies with classical bulges, the relation has a slope of 4.40 ± 0.32 and a smaller intrinsic scatter of 0.27 dex (red line in Figure 4). This result is very close to that of Kormendy & Ho (2013) (slope 4.38 ± 0.29 and intrinsic scatter 0.29 dex), who used a different fitting method than ours, verifying that our fitting results are robust with respect to fitting method. Our global $M_{\text{BH}} - \sigma$ relation (with all galaxies included) is likely to overestimate the black hole masses for pseudobulges and bulgeless galaxies, and therefore underestimate their Eddington ratios; conversely, ellipticals and classical bulges will have their black hole masses underestimated and Eddington ratios overestimated. While this situation is not ideal, it is the best we can do under the current circumstances.

When applying the $M_{\text{BH}} - \sigma$ relation, we use central stellar velocity dispersions, which are a reasonable

Table 3
X-ray AGN detection rates

Sample	Galaxies	X-ray Cores	Rate
Whole sample	719	314	44%
With optical classifications	418	243	58%
Optical Seyferts and LINERs	125	109	87%
Optical transition objects	41	28	68%
Optical H II nuclei	163	51	31%
Optical absorption-line nuclei	89	55	62%

proxy of bulge velocity dispersions (see Kormendy & Ho 2013). To be consistent with Ho (2008), we adopted the empirical bolometric correction for the X-ray band, $L_{\text{bol}} = 16 L_{\text{X}}$. Ho (2008) obtained this estimate based on broadband SEDs of LLAGNs, consistent with the result from Vasudevan & Fabian (2007), who suggested $L_{\text{bol}}/L_{\text{X}} = 15 - 25$ for AGNs with $L_{\text{bol}}/L_{\text{Edd}} < 0.1$. The Eddington ratio is then defined as $\lambda_{\text{Edd}} = 16 L_{\text{X}}/L_{\text{Edd}}$, where $L_{\text{Edd}} = 1.26 \times 10^{38} M_{\text{BH}}/M_{\odot} \text{ erg s}^{-1}$.

4. RESULTS AND DISCUSSION

Among the 719 galaxies in our *Chandra* sample, 314 are identified as AGN candidates (Table 2), including 228 that are located on the sky plane less than $1''$ from the near-infrared/optical nucleus. The total X-ray AGN fraction is 43.7%. Among the AGN candidates, optical spectral classifications are available for 243 (77%) objects, out of which 44% (106/243) are H II or absorption-line nuclei that do not show AGN signatures in the optical. Among galaxies previously recognized to contain H II nuclei, 31% (51/163) harbor an X-ray AGN candidate, and this fraction is 62% (55/89) for absorption-line nuclei. For optical Seyferts and LINERs, 87% (109/125) of them have an X-ray core. The X-ray AGN fraction is as high as $\sim 60\%$ for early-type (E–Sbc) galaxies and drops to $\sim 20\%$ in late types (Sc and later), consistent with previous results from optical surveys (Ho et al. 1997b; Ho 2008). We summarize the X-ray AGN detection rates in Table 3. A comprehensive analysis of AGN demographics will be given in R. She et al. (in preparation).

Spectral fitting can be performed for the AGN candidates that have sufficient counts. Among the 156 AGN spectra that meet this criterion, 84 can be adequately fitted with a single power-law model, and 65 with a powerlaw plus mekal model (a non-solar abundance for mekal is preferred in 5 cases). A partially covering absorbed power-law model (pcfabs*powerlaw) is more favored for 22 of them. An extragalactic absorption component is needed in 91 of the spectra. Other models (such as pexmon, powerlaw+tbody, and powerlaw+mekal+tbody) are used for very few cases. The best-fit models and parameters are shown in Table 4, where the errors are quoted at 90% confidence level. Figure 5 shows the fits for the individual objects. A statistically significant iron $K\alpha$ line, which we model with a simple Gaussian profile, is detected in 27 objects (Table 5).

The spectra of two sources (M 64 and M 100) can be well fitted with a single mekal component; no power-law component is needed. Figure 6 shows their radial profiles, compared with PSFs at the nuclear position, simulated with MARX, and radial profiles of nearby point-like

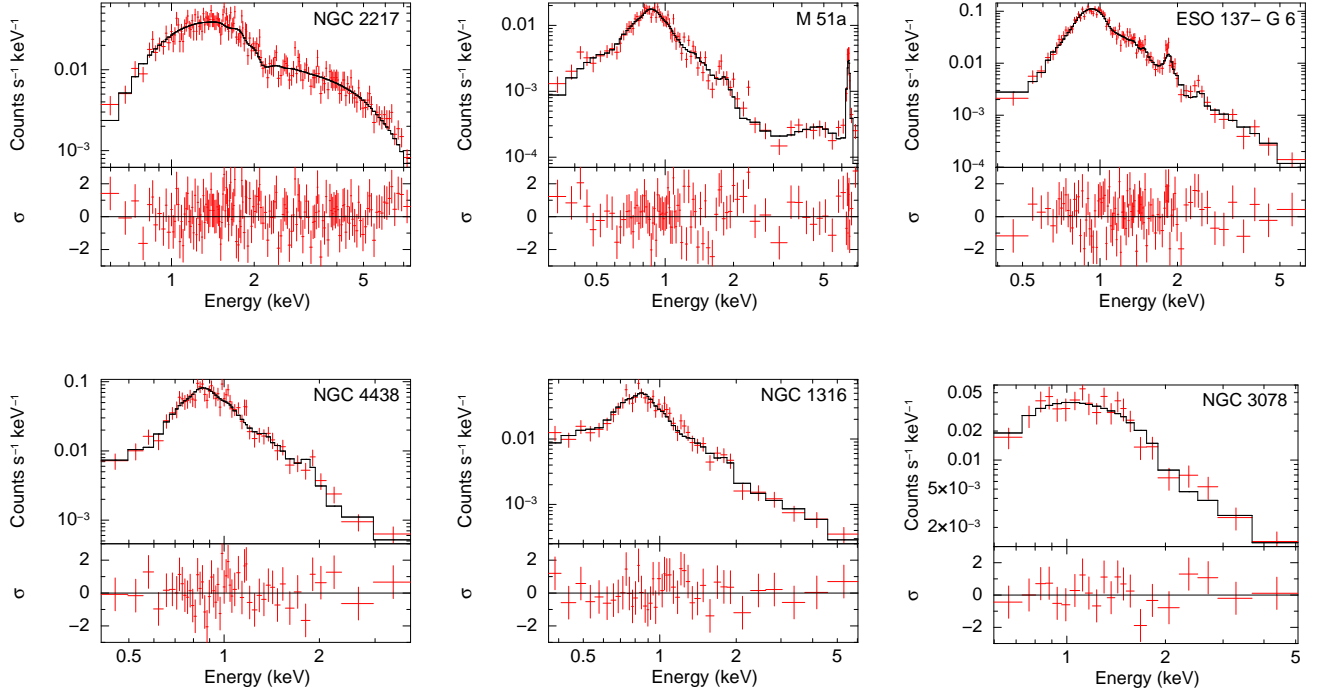


Figure 5. Spectral fits for the individual objects. Figure 5 is published in its entirety in electronic format. 6 objects are shown here for representatives.

Table 4
Fitting results of galaxies

ID	Name	Model	log Norm ₁	log L_{1} (erg s ⁻¹)	log Norm ₂	log L_{2} (erg s ⁻¹)	N_{H} (10 ²² cm ⁻²)	Γ	T (keV)	χ^2/dof	Note
(1)	(2)	(3)	(4)	(5)	(6)	(7)	(8)	(9)	(10)	(11)	(12)
10	Circinus Galaxy	pileup	430.00 ^{+40.00} -70.00	1.56 ^{+0.16} -0.51	Ref.2
15	ESO 137- G 6	PL+ME	-4.52	40.48	-3.84	40.90	0.12 ^{+0.04} -0.04	2.45 ^{+0.34} -0.34	0.75 ^{+0.03} -0.03	104.6/88	
21	ESO 428- G 14	PL+ME+BB+G	-4.61	40.37	-4.51	39.73	...	1.03 ^{+0.26} -0.27	0.69 ^{+0.10} -0.07	65.7/64	
24	ESO 495- G 21	PL+ME	-4.89	39.43	-4.61	38.74	...	0.66 ^{+0.28} -0.27	0.68 ^{+0.10} -0.05	44.8/33	
40	IC 342	PL+VME	-4.27	38.64	-3.74	38.68	...	1.92 ^{+0.21} -0.25	0.66 ^{+0.03} -0.03	142.6/106	
43	IC 750	PL	-5.17	39.50	2.30	...	5.2/3	
47	IC 1459	PL	-3.64	41.19	0.21 ^{+0.02} -0.02	1.86 ^{+0.06} -0.06	...	212.7/198	
51	IC 2560	PABS*PL+ME+G	-3.25	40.60	-4.74	39.67	22.41 ^{+7.28} -4.69	2.51 ^{+0.18} -0.26	0.19 ^{+0.04} -0.04	144.7/73	
88	IC 5267	PL+ME	-5.61	39.19	-5.49	38.75	...	1.46 ^{+0.59} -0.26	0.37 ^{+0.15} -0.06	5.6/7	
100	MCG -03-34-064	PABS*PL+ME+G	-2.59	42.58	-4.35	40.50	38.04 ^{+6.75} -5.97	1.89 ^{+0.16} -0.21	0.62 ^{+0.09} -0.20	63.8/48	
102	M 31	PL+ME	-4.14	37.56	-4.77	36.55	...	2.66 ^{+0.13} -0.14	0.22 ^{+0.05} -0.04	81.5/75	
103	M 32	PL	-5.02	36.58	2.60 ^{+0.20} -0.19	...	59.2/32	
105	M 49	PL+ME	-5.19	39.10	-4.57	39.44	...	2.27 ^{+0.17} -0.18	0.73 ^{+0.02} -0.04	100.1/80	
106	M 51a	PABS*PL+ME+G	-3.78	40.00	-5.03	38.33	35.16 ^{+8.44} -6.98	2.46 ^{+0.15} -0.17	0.64 ^{+0.03} -0.03	110.3/78	
107	M 51b	PL+ME	-5.20	38.83	-5.39	37.93	...	1.12 ^{+0.21} -0.20	0.78 ^{+0.25} -0.19	55.0/48	
108	M 58	PL	-2.90	41.80	1.39 ^{+0.05} -0.05	...	93.9/129	
109	M 59	PL	-5.15	39.30	0.06	1.80	...	1.4/4	
110	M 60	PL+ME	-6.04	38.57	-4.58	39.38	...	1.40 ^{+0.76} -2.45	1.08 ^{+0.04} -0.04	69.4/61	
111	M 61	PL+ME	-5.25	39.10	-5.60	38.27	...	1.53 ^{+0.46} -0.71	0.68 ^{+0.17} -0.24	6.3/6	
112	M 63	PL	-4.86	38.92	0.17 ^{+0.19} -0.15	1.96 ^{+0.52} -0.44	...	6.3/9	

Note. — Column 1: Source ID. Column 2: Galaxy names. Column 3: Models, see text for details. Here “PL”, “ME”, “VME”, “PABS”, “BB”, “G” denote powerlaw, mekal, vmekal, pcfabs, bbody, and gaussian (for iron $K\alpha$ line) component in XSPEC, respectively. Column 4: Normalization of powerlaw component in fitting model in units of photons $\text{keV}^{-1} \text{cm}^{-2} \text{s}^{-1}$. Column 5: Log of 0.3-10 keV luminosity of powerlaw component in fitting model. Column 6: Normalization of mekal or bbody component in fitting model, if available. It is equal to $(10^{-14}/4\pi D^2) \int n_e n_H dV$ for a mekal component, where D is the distance to the source, and n_e , n_H are the electron and hydrogen densities respectively. It is equal to L_{39}/D_{10}^2 for a bbody component, where L_{39} is the source luminosity in units of $10^{39} \text{ erg s}^{-1}$, and D_{10} is the distance to the source in units of 10 kpc. Column 7: Log of 0.3-10 keV luminosity of mekal or bbody component in fitting model, if available. Column 8: Intrinsic absorption column density. Column 9: Power-law photon index. In a few cases, the errors are not available due to poor statistics. Column 10: Temperature of the mekal or bbody component, if available. Column 11: χ^2 and the degree of freedom. Column 12: Note on spectral fitting or reference for pileup sources: Ref.1: Ebrero et al. (2011), Ref.2: De Rosa et al. (2012), Ref.3: Cappi et al. (2006), Ref.4: Shu et al. (2010), Ref.5: Iyomoto et al. (1998), Ref.6: Ptak et al. (2004), Ref.7: Weaver et al. (1999), Ref.8: Guainazzi et al. (2010), Ref.9: Evans et al. (2004). Table 4 is published in its entirety in the machine-readable format. A portion is shown here for guidance regarding its form and content.

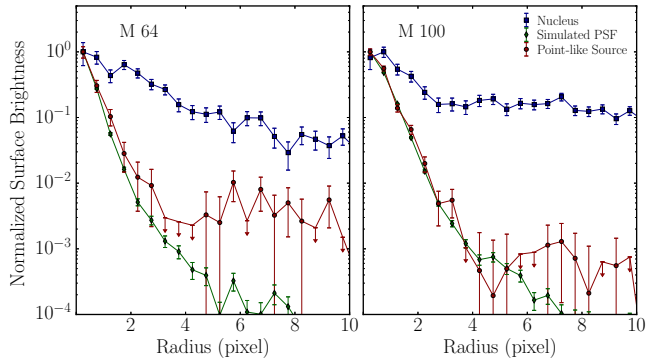


Figure 6. Radial profile for the nuclear X-ray source in M 64 (left) and M 100 (right), compared with a local PSF (simulated with MARX) and a nearby point-like object. They both show a single *mekal* spectrum and appear to be extended sources.

sources. They both appear to be spatially extended. We also examined their lightcurves and did not find any significant flux variability intra or inter observations (significance below 2σ). Thus, these two objects are not considered to be AGN candidates.

5. X-RAY PROPERTIES OF THE AGN CANDIDATES

5.1. Luminosity Functions

The cumulative luminosity functions (2–10 keV band) for the AGN candidates are shown in Figure 7, for the whole sample and separately for the different optical spectral classes. The luminosity functions for the whole sample and for Seyferts and LINERs seem to follow a broken power-law form. The small numbers of transition objects, H II nuclei, and absorption-line nuclei preclude a robust determination of their luminosity functions, but they are not inconsistent with a simple power-law.

5.2. Photon Index Distribution

Figure 8 plots the distribution of the photon index Γ for objects whose best-fit spectra include a power-law component with a degree of freedom (dof) greater than 5. Nearly 3/5 ($\sim 63\%$) of the objects have a Γ in the range of 1.3–2.3. The median value and standard deviation of Γ are 1.80 ± 0.52 . The standard deviation of the Γ distribution in this work is consistent with that in González-Martín et al. (2009, $\Gamma = 2.11 \pm 0.52$), but slightly larger than that in Bianchi et al. (2009, $\Gamma = 1.73 \pm 0.45$). We note that the sample in Bianchi et al. (2009) are all unobscured AGNs. If we exclude those objects with $N_{\text{H}} > 0.5 \times 10^{22} \text{ cm}^{-2}$ in our sample, the standard deviation of Γ becomes 0.46, consistent with the results of Bianchi et al. (2009). The discussion for Γ and AGN accretion states will be detailed in a forthcoming paper (She et al. in preparation).

6. CONTAMINATION BY X-RAY BINARIES

The AGN candidates, especially the low-luminosity sources, identified via near-infrared/optical and X-ray cross-correlation may be contaminated by other types of X-ray sources that are coincident with the galaxy nucleus. The most likely contaminants to LLAGNs are X-ray binaries. It is difficult to individually distinguish an LLAGN from a nuclear X-ray binary without deep

and/or long-term observations. Nevertheless, we argue that statistically the vast majority of these nuclear point-like X-ray sources are indeed AGNs.

As shown in Figure 3, the distribution of positional offsets between the stellar nucleus and the nearest X-ray source on the sky for all galaxies in our sample is bimodal. Our identified AGN candidates mostly occupy the first peak, consistent with little to no positional offset. This indicates that the nuclear X-ray sources belong to a population physically associated with the galaxy nuclei, ruling out the possibility that they belong to a distribution extended throughout the host galaxy that have been identified due to random coincidence with the nucleus. There are 228 AGN candidates located on the sky plane less than $1''$ to the near-infrared/optical nuclei. For comparison, the number density for point-like X-ray sources between $5''$ to $10''$ around the near-infrared/optical nuclear position is ~ 60 times lower in our sample galaxies. Of course, we cannot definitively rule out that our AGN candidates are accreting X-ray binaries residing within nuclear star clusters, a common component seen in late-type galaxies (e.g., Böker et al. 2002). For example, Feng et al. (2015) discovered a luminous X-ray flare from the nucleus of NGC 247, which could be due to an outburst from a low-mass X-ray binary in the nuclear star cluster.

The luminosity functions of the nuclear X-ray sources (Figure 7) also suggest that most of the candidates are AGNs. For comparison, the slope of the luminosity function is about -0.61 for high-mass X-ray binaries (Grimm et al. 2003) and around -1.1 for low-mass X-ray binaries (Kim & Fabbiano 2004). For ultraluminous X-ray sources, the slope is around -0.5 to -0.8 , depending on the choice of model (power-law or cutoff power-law) or the luminosity range (Swartz 2011), because their luminosity function rolls over and cuts off around $10^{41} \text{ erg s}^{-1}$. The luminosity function for our combined sample of all nuclear X-ray sources is much shallower than that of X-ray binaries, over the luminosity range in which they overlap. The luminosity function for the AGN candidates without line emission (absorption-line nuclei) do appear similar to that of ultraluminous X-ray sources. The nature of these sources will be discussed in depth in forthcoming papers.

6.1. Stacking Non-detections

To evaluate whether the vast majority of the AGN candidates are indeed AGNs, we performed a stacking analysis of the images for which no significant nuclear X-ray emission was detected in the individual exposures. For the non-detections, we stacked their exposure-corrected flux images centered at the near-infrared/optical position of each galaxy, after excising all nearby point-like sources detected by *wavdetect*. We excluded those images on which a point-like source was detected within $5''$ radius from the galaxy nucleus; these images may contaminate the central region. Our final stack contains images of 368 non-detections, with a total exposure time of 6935.2 ks. The stacked 0.3–8 keV flux image, shown in Figure 9, reveals a statistically significant source with a net photon flux of $5.1 \times 10^{-7} \text{ photon cm}^{-2} \text{ s}^{-1}$ from an aperture of $2''$ radius and background from an annulus with inner and outer radii of $15''$ and $25''$, respectively. This corresponds to a flux of $8.9 \times 10^{-16} \text{ erg cm}^{-2} \text{ s}^{-1}$, given a power-law model with a photon index $\Gamma = 1.8$

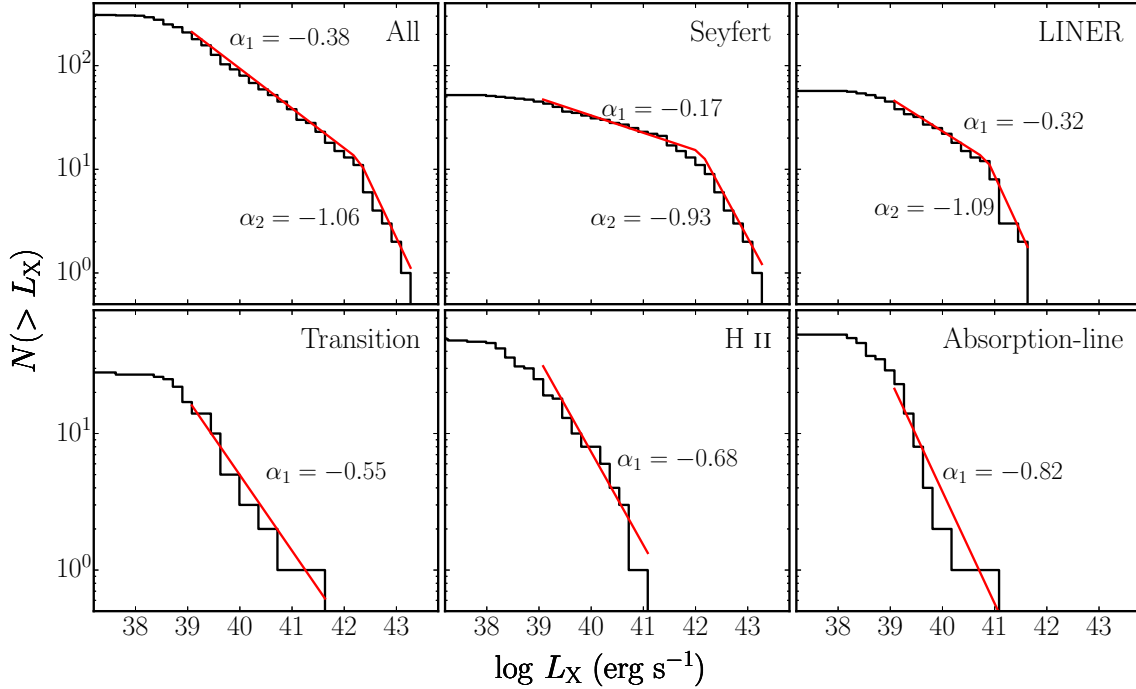


Figure 7. Cumulative luminosity distribution (2–10 keV band) for AGN candidates in our sample. The red line is the fit to a broken power-law or a single power-law model at luminosities above 10^{39} erg s $^{-1}$.

Table 5
Objects with iron K α line

Name	EW (eV)	Ref	Name	EW (eV)	Ref	Name	EW (eV)	Ref
Circinus Galaxy	2250	Ref.2	NGC 1365	170		NGC 4939	232	
ESO 428- G 14	3041		NGC 1386	2407		NGC 4945	1140	
IC 2560	3319		NGC 2110	88		NGC 5128	82	Ref.9
MCG -03-34-064	636		NGC 2782	629		NGC 5347	521	
M 51a	4793		NGC 2992	255	Ref.4	NGC 5506	130	Ref.8
M 77	1200	Ref.3	NGC 3079	95		NGC 5728	886	
M 81	40	Ref.3	NGC 4051	240	Ref.3	NGC 6300	140	Ref.2
NGC 253	851		NGC 4151	300	Ref.3	NGC 7172	76	Ref.2
NGC 1052	300	Ref.7	NGC 4388	434		NGC 7479	35	

Note. — Reference codes are in Table 4.

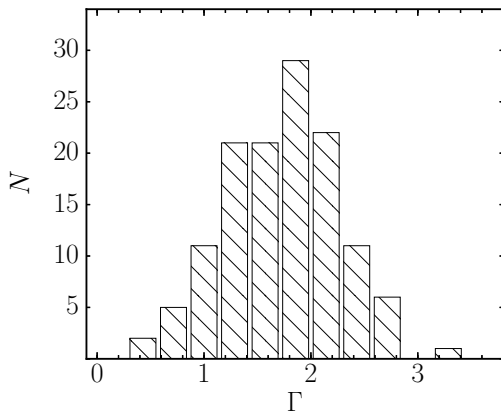


Figure 8. Distribution of the power-law photon index Γ in the 0.3–8 keV band, for AGN candidates whose best-fit model includes a power-law component and has a dof > 5 .

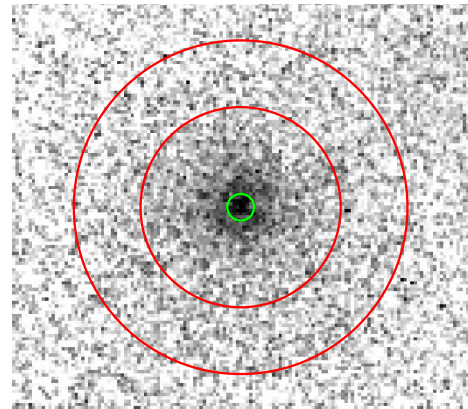


Figure 9. Stacked image of 368 non-detections, in the energy range 0.3–8 keV. The green circle (2'' radius) is the source aperture, and the red annulus is the background region used to calculate source flux.

and a typical Galactic absorption $N_{\text{H},0}=2 \times 10^{20} \text{ cm}^{-2}$. The aperture size was chosen in view of the fact that the typical PSF radius of *Chandra*/ACIS is less than $1''$, the absolute astrometry is better than $1''$, and most of the source extracting regions given by *wavdetect* have a radius less than $2''$. The flux will be 3 times higher if an aperture with a radius of $5''$ is used. To evaluate if observations with different exposures and backgrounds will bias the sensitivity, we split all non-detections into several subsets depending on their exposure times and performed the same stacking analysis. The derived flux from different subsets follows $F \propto t^{-1/2}$, where t is total exposure of the subset, suggesting that there is no significant bias from stacking both shallower and deeper exposures. We checked the stacked images in two bands, 0.3–2 and 2–8 keV, and found that the fluxes of the X-ray excess in these two bands are consistent with emission from such an absorbed power-law model, but inconsistent with emission from hot gas (*mekal* with a temperature of 0.4–0.9 keV). At the typical distance of 17 Mpc for the 368 galaxies with non-detections, this yields an average X-ray luminosity of $3.1 \times 10^{37} \text{ erg s}^{-1}$. This luminosity is broadly consistent with that of an X-ray binary, and thus this emission can be accounted for by an ensemble of low-luminosity X-ray binaries. The spatial extension of the X-ray excess ($R \sim 5''$) is also larger than the concentration of the detected AGNs (mostly within $1''$), suggesting that they are likely X-ray sources associated with the nuclear stellar component.

The above results further strengthen our argument that the X-ray-detected nuclear sources do not suffer significantly from contamination by X-ray binaries or emission from hot gas. The above calculated average luminosity contributes only $\sim 1\%$ of a typical AGN candidate luminosity (0.3–8 keV; $2.5 \times 10^{39} \text{ erg s}^{-1}$) in this work.

We thank the anonymous referee for his/her insightful suggestions to improve this paper. The work of LCH is supported by National Key Program for Science and Technology Research and Development grant 2016YFA0400702. HF acknowledges funding support from the National Natural Science Foundation of China under grant No. 11633003, and the Tsinghua University Initiative Scientific Research Program. This research has made use of the NASA/IPAC Extragalactic Database (NED) which is operated by the Jet Propulsion Laboratory, California Institute of Technology, under contract with the National Aeronautics and Space Administration. We also acknowledge the usage of the HyperLeda database (<http://leda.univ-lyon1.fr>).

REFERENCES

- Akritas, M. G., & Bershadsky, M. A. 1996, *ApJ*, 470, 706
 Alexander, D. M., & Hickox, R. C. 2012, *New A Rev.*, 56, 93
 Arnaud, K. A. 1996, in *Astronomical Society of the Pacific Conference Series*, Vol. 101, *Astronomical Data Analysis Software and Systems V*, ed. G. H. Jacoby & J. Barnes, 17
 Barth, A. J., Ho, L. C., Rutledge, R. E., & Sargent, W. L. W. 2004, *ApJ*, 607, 90
 Bianchi, S., Guainazzi, M., Matt, G., Fonseca Bonilla, N., & Ponti, G. 2009, *A&A*, 495, 421
 Böker, T., Laine, S., van der Marel, R. P., et al. 2002, *AJ*, 123, 1389
 Bruzual, G., & Charlot, S. 2003, *MNRAS*, 344, 1000
 Cappi, M., Panessa, F., Bassani, L., et al. 2006, *A&A*, 446, 459
 Colless, M., Peterson, B. A., Jackson, C., et al. 2003, arXiv:astro-ph/0306581
 Davis, J. E., Bautz, M. W., Dewey, D., et al. 2012, in *Proc. SPIE*, Vol. 8443, *Space Telescopes and Instrumentation 2012: Ultraviolet to Gamma Ray*, 84431A
 den Brok, M., Seth, A. C., Barth, A. J., et al. 2015, *ApJ*, 809, 101
 De Rosa, A., Panessa, F., Bassani, L., et al. 2012, *MNRAS*, 420, 2087
 Desroches, L.-B., & Ho, L. C. 2009, *ApJ*, 690, 267
 de Vaucouleurs, G., de Vaucouleurs, A., Corwin, H. G., et al. 1991, *Third Reference Catalogue of Bright Galaxies*. (Springer)
 Dong, X.-B., Ho, L. C., Yuan, W., et al. 2012, *ApJ*, 755, 167
 Driver, S. P., Hill, D. T., Kelvin, L. S., et al. 2011, *MNRAS*, 413, 971
 Dudik, R. P., Satyapal, S., Gliozzi, M., & Sambruna, R. M. 2005, *ApJ*, 620, 113
 Dudik, R. P., Satyapal, S., & Marcu, D. 2009, *ApJ*, 691, 1501
 Ebrero, J., Costantini, E., Kaastra, J. S., de Marco, B., & Dadina, M. 2011, *A&A*, 535, A62
 Evans, D. A., Kraft, R. P., Worrall, D. M., et al. 2004, *ApJ*, 612, 786
 Falco, E. E., Kurtz, M. J., Geller, M. J., et al. 1999, *PASP*, 111, 438
 Feng, H., Ho, L. C., Kaaret, P., et al. 2015, *ApJ*, 807, 185
 Feng, H., & Soria, R. 2011, *New A Rev.*, 55, 166
 Ferrarese, L., & Merritt, D. 2000, *ApJ*, 539, L9
 Filho, M. E., Barthel, P. D., & Ho, L. C. 2006, *A&A*, 451, 71
 Filippenko, A. V., & Ho, L. C. 2003, *ApJ*, 588, L13
 Gallo, E., Treu, T., Jacob, J., et al. 2008, *ApJ*, 680, 154
 Gallo, E., Treu, T., Marshall, P. J., et al. 2010, *ApJ*, 714, 25
 Gebhardt, K., Bender, R., Bower, G., et al. 2000, *ApJ*, 539, L13
 Gebhardt, K., Lauer, T. R., Kormendy, J., et al. 2001, *AJ*, 122, 2469
 González-Martín, O., Masegosa, J., Márquez, I., Guainazzi, M., & Jiménez-Bailón, E. 2009, *A&A*, 506, 1107
 Goulding, A. D., & Alexander, D. M. 2009, *MNRAS*, 398, 1165
 Greene, J. E. 2012, *NatCo*, 3, 1304
 Greene, J. E., & Ho, L. C. 2004, *ApJ*, 610, 722
 Greene, J. E., & Ho, L. C. 2007, *ApJ*, 670, 92
 Greene, J. E., & Ho, L. C. 2009, *PASP*, 121, 1167
 Greene, J. E., Seth, A., Kim, M., et al. 2016, *ApJ*, 826, L32
 Grimm, H.-J., Gilfanov, M., & Sunyaev, R. 2003, *MNRAS*, 339, 793
 Gu, Q., Melnick, J., Cid Fernandes, R., et al. 2006, *MNRAS*, 366, 480
 Guainazzi, M., Bianchi, S., Matt, G., et al. 2010, *MNRAS*, 406, 2013
 Haehnelt, M. G., & Rees, M. J. 1993, *MNRAS*, 263, 168
 Heckman, T. M. 1980, *A&A*, 87, 152
 Heckman, T. M., & Best, P. N. 2014, *ARA&A*, 52, 589
 Heger, A., Fryer, C. L., Woosley, S. E., Langer, N., & Hartmann, D. H. 2003, *ApJ*, 591, 288
 Ho, L. C. 2008, *ARA&A*, 46, 475
 Ho, L. C. 2009, *ApJ*, 699, 626
 Ho, L. C., Filippenko, A. V., & Sargent, W. L. W. 1993, *ApJ*, 417, 63
 Ho, L. C., Filippenko, A. V., & Sargent, W. L. W. 1997a, *ApJS*, 112, 315
 Ho, L. C., Filippenko, A. V., & Sargent, W. L. W. 1997b, *ApJ*, 487, 568
 Ho, L. C., Filippenko, A. V., & Sargent, W. L. W. 2003, *ApJ*, 583, 159
 Ho, L. C., Greene, J. E., Filippenko, A. V., & Sargent, W. L. W. 2009, *ApJS*, 183, 1
 Ho, L. C., Feigelson, E. D., Townsley, L. K., et al. 2001, *ApJ*, 549, L51
 Iyamoto, N., Makishima, K., Matsushita, K., et al. 1998, *ApJ*, 503, 168
 Jacoby, G. H., Branch, D., Ciardullo, R., et al. 1992, *PASP*, 104, 599
 Jarrett, T. H., Chester, T., Cutri, R., et al. 2000, *AJ*, 119, 2498
 Jones, D. H., Read, M. A., Saunders, W., et al. 2009, *MNRAS*, 399, 683
 Kalberla, P. M. W., Burton, W. B., Hartmann, D., et al. 2005, *A&A*, 440, 775
 Kelly, B. C. 2007, *ApJ*, 665, 1489
 Kennicutt, Jr., R. C. 1992, *ApJS*, 79, 255
 Kim, D.-W., & Fabbiano, G. 2004, *ApJ*, 611, 846
 Kormendy, J., & Ho, L. C. 2013, *ARA&A*, 51, 511
 Kormendy, J., & Kennicutt, Jr., R. C. 2004, *ARA&A*, 42, 603
 Kormendy, J., & Richstone, D. 1995, *ARA&A*, 33, 581
 Magorrian, J., Tremaine, S., Richstone, D., et al. 1998, *AJ*, 115, 2285
 Merritt, D., Ferrarese, L., & Joseph, C. L. 2001, *Science*, 293, 1116
 Miller, B., Gallo, E., Treu, T., & Woo, J.-H. 2012, *ApJ*, 747, 57
 Miller, B. P., Gallo, E., Greene, J. E., et al. 2015, *ApJ*, 799, 98

- Moustakas, J., & Kennicutt, Jr., R. C. 2006, *ApJS*, 164, 81
- Peterson, B. M., Bentz, M. C., Desroches, L.-B., et al. 2005, *ApJ*, 632, 799
- Ptak, A., Terashima, Y., Ho, L. C., & Quataert, E. 2004, *ApJ*, 606, 173
- Rosales-Ortega, F. F., Kennicutt, R. C., Sánchez, S. F., et al. 2010, *MNRAS*, 405, 735
- Sarzi, M., Falcón-Barroso, J., Davies, R. L., et al. 2006, *MNRAS*, 366, 1151
- Satyapal, S., Vega, D., Dudik, R. P., Abel, N. P., & Heckman, T. 2008, *ApJ*, 677, 926
- Shu, X. W., Yaqoob, T., Murphy, K. D., et al. 2010, *ApJ*, 713, 1256
- Skrutskie, M. F., Cutri, R. M., Stiening, R., et al. 2006, *AJ*, 131, 1163
- Swartz, D. A. 2011, *Astronomische Nachrichten*, 332, 341
- Terashima, Y., & Wilson, A. S. 2003, *ApJ*, 583, 145
- Vasudevan, R. V., & Fabian, A. C. 2007, *MNRAS*, 381, 1235
- Véron-Cetty, M.-P., & Véron, P. 2010, *A&A*, 518, A10
- Volonteri, M., Lodato, G., & Natarajan, P. 2008, *MNRAS*, 383, 1079
- Weaver, K. A., Wilson, A. S., Henkel, C., & Braatz, J. A. 1999, *ApJ*, 520, 130
- Weisskopf, M. C., Brinkman, B., Canizares, C., et al. 2002, *PASP*, 114, 1
- Yuan, F., & Narayan, R. 2014, *ARA&A*, 52, 529
- Zhang, W. M., Soria, R., Zhang, S. N., Swartz, D. A., & Liu, J. F. 2009, *ApJ*, 699, 281